Journal of Computational Physics 271 (2014) 151–171

Contents lists available at ScienceDirect

Journal of Computational Physics

www.elsevier.com/locate/jcp

Modeling of ocean–atmosphere interaction phenomena during the breaking of modulated wave trains

A. Iafrati [a,*], A. Babanin [b], M. Onorato [c]

[a] INSEAN–CNR, Marine Technology Research Institute, Rome, Italy
[b] Swinburne University of Technology, Melbourne, Australia
[c] University of Turin, Turin, Italy

ARTICLE INFO

Article history:
Received 19 May 2013
Received in revised form 10 December 2013
Accepted 21 December 2013
Available online 2 January 2014

Keywords:
Modulational instability
Ocean atmosphere interaction
Potential flow methods
Two-fluids flows
Level-set methods
Vortex dynamics

ABSTRACT

Air water interaction phenomena taking place during the breaking of ocean waves are investigated here. The study is carried out by exploiting the combination between a potential flow method, which is used to describe the evolution of the wave system up to the onset of the modulational instability, and a two-fluids Navier–Stokes solver which describes the strongly non-linear air–water interaction taking place during breaking events. The potential flow method is based on a fully non-linear mixed Eulerian–Lagrangian approach, whereas the two-fluid model uses a level-set method for the interface capturing. The method is applied to study the evolution of a modulated wave train composed by a fundamental wave component with two side band disturbances. It is shown that breaking occurs when the initial steepness exceed a threshold value. Once the breaking starts, it is not just a single event but it is recurrent with a period associated to the group velocity. Results are presented in terms of free surface shapes, velocity and vorticity fields, energy and viscous dissipation. The analysis reveals the formation of large vortex structures in the air domain which are originated by the separation of the air flow at the crest of the breaking wave. The form drag associated to the flow separation process significantly contributes to the dissipation of the energy content of the wave system. The energy fraction dissipated by each breaking event is distinguished.

1. Introduction

Breaking of surface waves, as an oceanic phenomenon, has many important implications. Scientifically, these are the problems of wave dynamics, atmospheric boundary layer, air–sea-interactions, upper ocean turbulence mixing, with respective connections to the large-scale processes including ocean circulation, weather and climate. In engineering, these are naval architecture, structural design of offshore developments and pipelines, coastal and bottom erosion, marine transportation, navigation, among many others [1].

The wave breaking process has received a considerable interest over the last decades, and some of the main features such as characteristics of the breaking onset and probability of breaking, have been described, quantified and parameterized (see e.g. [2] for a review). Much less has been done with respect to the breaking severity and to the air–water interaction phenomena taking place during the breaking event, which are the topics addressed in the present paper.

If the breaking strength is defined as energy loss in a single breaking event, then the breaking severity coefficient can be identified in a number of ways, that is through the measurements of the individual breaking wave, of the group where

* Corresponding author.
E-mail address: alessandro.iafrati@cnr.it (A. Iafrati).

0021-9991/$ – see front matter
http://dx.doi.org/10.1016/j.jcp.2013.12.045

the breaking occurred, of spectra of the respective group before and after the breaking. Magnitude of such coefficient varies greatly, virtually from 0% to 100%.

Such wide range of variation cannot be disregarded or substituted with some mean value in applications which involve the breaking severity. This is for example the case of the wave-energy dissipation function employed in wave forecast models. It can in principle be directly determined as a product of the breaking probability and breaking severity, but without reliable parameterizations of the latter, a set of inventive indirect, usually speculative, methods have been elaborated to estimate the dissipation function [3].

The waves break when they reach some critical steepness at which the water surface becomes unstable and inevitably collapses [4,5]. A significant number of processes in the ocean can make this happen, e.g. hurricane wind-forcing, surface currents with horizontal velocity gradients, bottom proximity, modulation of long waves by short waves, among others. In typical background deep-water oceanic conditions for dominant waves, however, these processes are two: linear superposition and modulational instability [6].

Most of the research studies of the wave breaking process in controlled laboratory conditions was done for the linear-superposition scenario. Classical work of [7] concludes for such wave-breaking strength: "The loss of excess momentum flux and energy flux was measured and found to range from 10% for single spilling events to as much as 25% for plunging breakers". That is, in such case the breaking severity is some limited fraction of the pre-breaking wave energy. In [8] similar conclusions were derived by using the two-fluids Navier–Stokes solver.

Remarkably different is wave-breaking severity in case of breaking caused by the modulational instability. In [9] it was demonstrated that it can be anything, from virtually 0%, i.e. a mere toppling the wave crest, to 100%, i.e. the breaking wave disappears. In fact, it can be shown that due to the modulational instability, the wave steepness can be significantly amplified up to three times the initial value, depending on the spectrum [10]. With such amplification effect, even apparently gentle wave system may break.

Despite such interest, only few laboratory studies have investigated the breaking originated by modulational instability, e.g. [11]. Numerically, the attention was focused to the identification of the conditions for the onset of the breaking by using weakly or fully non-linear potential flow methods, e.g. [12,13], but, to the authors knowledge, nothing is available for the breaking phase.

The description of the breaking process requires a model which can account for possible topological changes of the interface as well as for the air–water interaction processes. This is possible by using a two-fluid model which has been already used in the past to investigate the breaking obtained by linear-superposition [8,14].

The use of such highly expensive computational tools has to be limited in space and time. Even with large supercomputers available, simulations cannot span over all the scales ranging from the hundreds of kilometers, needed to describe the wave generation under the action of the wind in open ocean, up to the finest whitecaps detail with tiny drops and bubbles. But even focusing the attention to a basic problem like the instability of a modulated wave train, large computational domains (several fundamental wavelengths) are required for an accurate description of the wave dynamics and, moreover, very long time intervals, up to hundreds of wave periods, are needed for the development of the instability and for the onset of the breaking. The use of two-fluids numerical methods for such long intervals is too expensive from the computational viewpoint and, moreover, unless a highly refined discretization is adopted, there is the possibility that little amount of artificial dissipation of the numerical scheme, accumulated over long integration times, may prevent the development of the instability [15].

The common practice in wave forecasting is to use spectral approaches with ideal fluid assumption, in which a dissipation term is introduced to account for the breaking occurrence. A rather recent example is [16]. However, there is evidence that such dissipation term deserves a deeper investigation, e.g. [3,9,17]. This gave the motivation to undertake a study in which a potential flow model is used to describe the wave dynamics up to the onset of the breaking and then the solution is passed to a two-fluid solver to describe the breaking phase. The final aim is to derive an improved parameterization of the breaking dissipation which can relate the pre-breaking spectrum to the energy dissipation and to the post-breaking spectrum. In the present work, a fully non-linear potential flow model is adopted in a first stage during which the modulational instability develops. At the onset of the breaking, the potential flow solution is used to compute the velocity field in the air and water and to start the two-fluids simulation. It is worth remarking that both computational models use a two-dimensional assumption. Note that the initialization procedure adopted here can be used without any relevant change, in combination with spectral approaches. The fully non-linear method was preferred as it better identifies the breaking occurrence.

The combined method is applied to the study of the modulational instability of a fundamental wave with two side bands components. The analysis follows the development of the instability for different values of the initial steepness of the fundamental component, and two-fluids numerical simulations are used from a time just before the onset of the breaking. Results are presented in terms of free surface shape, velocity and vorticity fields and energy dissipation. It is worth noticing that some results have been already presented in [18]. Therein, the energy amount transferred in air as a consequence of the dipolar formation is analyzed and it is shown that, in the simulation period, the integrated energy dissipation in air is about twice that in water. The result is found to be almost independent of the wave steepness. Here a more detailed discussion of the computational approach and several additional physical aspects are provided.

2. Combined numerical model

2.1. Fully non-linear potential flow model

Up to the breaking occurrence, the evolution of a modulated wave train can be accurately and efficiently described within the potential flow assumption, provided all the non-linearities in the dynamic and kinematic boundary conditions are accounted for. The flow in water is expressed in terms of a velocity potential $\phi(x, y, t)$ which satisfies the Laplace equation within the liquid domain, the impermeability constraint at the bottom S_B and the dynamic and kinematic conditions at the free surface S_F. This is expressed by the following boundary value problem

$$\nabla^2\phi = 0 \quad \text{in } \Omega, \tag{1}$$

$$\frac{\partial\phi}{\partial n} = 0 \quad \text{on } S_B, \tag{2}$$

$$\frac{D\phi}{Dt} = -\frac{y}{Fr^2} + \frac{|\nabla\phi|^2}{2} \quad \text{on } S_F, \tag{3}$$

$$\frac{D\boldsymbol{x}}{Dt} = \nabla\phi \quad \text{on } S_F \tag{4}$$

where Ω denotes the water domain and $\boldsymbol{n}$ the unit vector normal to the surface, oriented inwards. In the above equation Fr indicates the Froude number which is defined as

$$Fr = \frac{U_r}{\sqrt{gL_r}},$$

where U_r and L_r are reference values for velocity and length, respectively. The y-axis is vertical and oriented upwards.

For the problems discussed herewith, periodic boundary conditions are assigned at the lateral boundaries of the computational domain S_D. Note that the surface tension contribution is missing in the dynamic boundary condition. Neglecting that term can be justified by the fact that, for the range of wavelengths considered in the present paper, as long as the wave train remains regular, the interface curvature is small and the surface tension gives a inappreciable contribution.

The time dependent boundary value problem (1)–(4) is solved by using a mixed Eulerian–Lagrangian approach [19] which was carefully validated in water entry flows [20,21]. At each time step, the solution of the boundary value problem for the velocity potential is sought in the form of a boundary integral representation of the velocity potential, which is

$$\phi(\boldsymbol{x}_P) = \int\limits_{S_B\cup S_F\cup S_D} \left(\phi(\boldsymbol{x}_Q)\frac{\partial G(\boldsymbol{x}_P-\boldsymbol{x}_Q)}{\partial n_Q} - \frac{\partial\phi(\boldsymbol{x}_Q)}{\partial n_Q}G(\boldsymbol{x}_P-\boldsymbol{x}_Q)\right)\mathrm{d}S_Q \quad (\boldsymbol{x}_P\in\Omega) \tag{5}$$

where $G(\boldsymbol{x}_P-\boldsymbol{x}_Q)$ is the free-space Green's function of the Laplace operator in two-dimensions. In presence of a flat and horizontal bottom located at $y = y_B$ ($y_B < 0$), the image effect is exploited by using the Green's function

$$G^*(\boldsymbol{x}_P-\boldsymbol{x}_Q) = \frac{1}{2\pi}\left[\log\left(|\boldsymbol{x}_P-\boldsymbol{x}_Q|\right) + \log\left(|\boldsymbol{x}_P-\boldsymbol{x}_Q^*|\right)\right], \tag{6}$$

where $\boldsymbol{x}_Q = (x_Q, y_Q)$ and $\boldsymbol{x}_Q^* = (x_Q, 2y_B - y_Q)$.

According to the boundary value problem stated by Eqs. (1)–(4), the velocity potential is assigned on the free surface S_F. Additional conditions are enforced at the two periodic boundaries, assuming that the velocity potential takes the same values on the two sides whereas, due to the change in the orientation of the normal, its normal derivative takes the same values but opposite sign. Those values are both unknown and are determined by the solution of the boundary value problem.

The boundary value problem is solved by taking the limit of the boundary integral representation (5) as $\boldsymbol{x}_P$ approaches the boundary of the water domain $\partial\Omega$. For smooth contours the limit process provides:

$$\frac{1}{2}\phi_P - \int\limits_{S_D}\left(\phi_Q\frac{\partial G^*_{PQ}}{\partial n_Q} - \frac{\partial\phi_Q}{\partial n_Q}G^*_{PQ}\right)\mathrm{d}S_Q + \int\limits_{S_F}\frac{\partial\phi_Q}{\partial n_Q}G^*_{PQ}\,\mathrm{d}S_Q = +\int\limits_{S_F}\phi_Q\frac{\partial G^*_{PQ}}{\partial n_Q}\,\mathrm{d}S_Q\,. \tag{7}$$

In the above equation ϕ_P denotes $\phi(\boldsymbol{x}_P)$ and similarly, G^*_{PQ} is used for $G^*(\boldsymbol{x}_P-\boldsymbol{x}_Q)$.

The solution of the integral equation (7) provides the normal derivative of the velocity potential on the free surface S_F, which, together with the velocity potential ϕ, allows to derive the velocity field on the free surface as:

$$\boldsymbol{u} = \phi_\tau\boldsymbol{\tau} + \phi_n\boldsymbol{n}, \tag{8}$$

where ϕ_τ and ϕ_n denote the tangential and normal derivatives of the velocity potential at the free surface, respectively. The velocity field (8) is used in the time integration of Eqs. (3) and (4) which provide the new free surface shape and the distribution of the velocity potential on it.

The boundary integral equation is solved numerically by discretizing the fluid boundary into straight line segments. Along each segment, the velocity potential and its normal derivative are assumed to be piecewise constant, and equal to the value they take at the centroid of the segment. The integration in time of Eqs. (3) and (4) is conducted by a second order accurate scheme. At each iteration, the time step is chosen so that, for any centroid, the displacement is always less than one fourth the corresponding panel length. With the centroid positions at the next step available, the vertices of the segments are located by passing a cubic spline through the centroids. The vertices of the segments are located along the spline curve at the midpoint between two successive centroids [20].

In the discrete solution of the boundary value problem with periodic boundary conditions, a significant improvement in the accuracy of the periodic condition has been achieved by formulating the problem on a computational domain which is three times wider that the basic periodic domain. Hence, the solution computed in the central portion is copied to the left and right portions to have the solution in the entire domain.

2.2. Two-fluids Navier–Stokes solver

The fully non-linear potential flow approach cannot be used after the onset of the breaking. A first limit is related to the difficulty in handling possible topological changes in the free surface that may occur during the breaking process. Furthermore, in presence of breaking, vorticity is generated both by viscous effects or by the topological change of the interface in case of bubble entrainment processes [14]. All the above effects, as well as the air–water interaction taking place during the breaking process may be more appropriately described by a two-fluids approach.

The literature in the field of two-fluid models is rather wide, e.g. [22–24], just to mention few examples. In the present work we adopt a model which has been already validated and widely used in the context of the wave breaking modeling at different length scales [8,14,25]. As the model has been already presented and validated in previous studies, here only the key points of the method are recalled whereas a deeper description of the numerical scheme and of its validation can be found in [25,26] and in [8].

The two-fluids flow of air and water is approximated as that of a single incompressible fluid whose density and viscosity vary smoothly across the interface. The governing equations are written in generalized stationary coordinates [27] as follows:

$$\frac{\partial U_m}{\partial \xi_m} = 0, \tag{9}$$

$$\frac{\partial}{\partial t}\left(J^{-1}u_i\right) + \frac{\partial}{\partial \xi_m}(U_m u_i) = -\frac{1}{\varrho}\frac{\partial}{\partial \xi_m}\left(J^{-1}\frac{\partial \xi_m}{\partial x_i}p\right) - J^{-1}\frac{\delta_{i2}}{Fr^2} - \frac{\kappa}{\varrho We^2}\frac{\partial}{\partial \xi_m}\left(J^{-1}\frac{\partial \xi_m}{\partial x_i}H_{\delta_T}(d)\right) + \frac{1}{\varrho Re}\frac{\partial}{\partial \xi_m}\left(\mu G^{ml}\frac{\partial u_i}{\partial \xi_l} + \mu B^{mlji}\frac{\partial u_j}{\partial \xi_l}\right). \tag{10}$$

In the above equations u_i is the i-th Cartesian velocity component, δ_{ij} is the Kronecker delta,

$$U_m = J^{-1}\frac{\partial \xi_m}{\partial x_j}u_j \tag{11}$$

is the volume flux normal to the $\xi_m = const.$ surface and J^{-1} is the inverse of the Jacobian. Non-dimensional ratios are defined as

$$Re = \frac{U_r L_r \varrho_w}{\mu_w}, \qquad We = U_r\sqrt{\frac{\varrho_w L_r}{\sigma}}$$

for Reynolds and Weber numbers, respectively. Again, U_r and L_r are reference values for velocity and length, σ is the surface tension coefficient, ϱ_w and μ_w are the values of the density and dynamic viscosity of water, respectively. These values are also used as reference values for the non-dimensionalization of the corresponding quantities. In Eq. (10) G^{ml} and B^{mlji} are metric quantities and κ is the local curvature.

The jump in the fluid properties at the free surface, as well as the surface tension forces, are spread across a small neighborhood of the interface. This is achieved through a smoothed Heaviside function $H_\delta(d)$, where d is the signed distance from the interface, assumed to be positive in water and negative in air.

Cartesian velocities and pressure are defined at the cell centers, whereas volume fluxes are defined at the mid-point of the cell faces. The solution is advanced in time through a fractional step approach in which the pressure contribution is neglected when integrating the momentum equation in time (*Predictor step*) and it is reintroduced in the next stage (*Corrector step*) when the continuity of the velocity field is enforced. In order to reduce the constraints of the related stability limit, the diagonal part of the first viscous contribution in (10) is computed implicitly with a Crank–Nicholson scheme, whereas all other terms are computed explicitly with a three-steps low storage Runge–Kutta scheme.

The pressure corrector Φ is derived by enforcing the continuity of the velocity field at the end of the substep [25]. This yields a Poisson equation

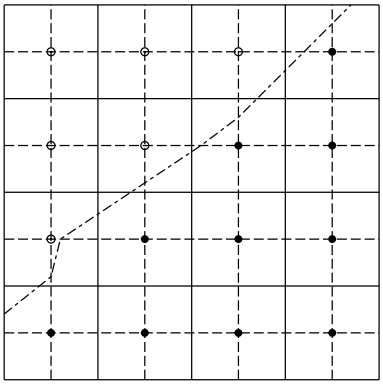

Fig. 1. Sketch of the procedure adopted to locate the interface. Solid lines are used to mark the cells whereas dashed lines are used for the staggered cell system defined by the cell centers. The distance is defined at the cell centers, with full and empty circles distinguishing centers where the distance is positive and negative, respectively. The interface (*dash-dotted*) is built by connecting the intersections of the bilinear interpolation of the distance function with the boundaries of the staggered cells.

$$\frac{\partial}{\partial\xi_m}\left(\frac{G^{mj}}{\varrho^l}\frac{\partial\Phi^l}{\partial\xi_j}\right)=\frac{1}{\Delta t}\frac{\partial\hat{U}^l_m}{\partial\xi_m}-\frac{\zeta_{l-1}}{\gamma_l}\frac{\partial}{\partial\xi_m}\left(\frac{G^{mj}}{\varrho^{l-1}}\frac{\partial\Phi^{l-1}}{\partial\xi_j}\right), \tag{12}$$

where the superscript l denotes the substep index of the third order Runge–Kutta scheme, and ζ, γ are time advancing coefficients. The Poisson equation is solved by using a BiCGStab algorithm, in combination with an Incomplete LU decomposition for the preconditioning.

The interface between air and water is captured as the zero level-set of a signed normal distance from the interface $d(\boldsymbol{x}, t)$ which, at $t = 0$, is initialized by assuming $d > 0$ in water, $d < 0$ in air. Physical fluid properties are related to d by the equation:

$$f(d) = f_a + (f_w - f_a)H_\delta(d) \tag{13}$$

where the parameter δ is chosen so that the density and viscosity jumps are spread across five grid cells, at least [25]. The distance function is advected in time with the flow as a non-diffusive scalar by using the equation

$$\frac{\partial d}{\partial t} + \boldsymbol{u}\cdot\nabla d = 0. \tag{14}$$

The integration in time of the above equation is carried out with the same scheme employed for the convective terms. At the end of each time step, the interface location is identified as the zero level of the updated field $d(\boldsymbol{x}, t)$. The function d being defined at the cell centers, in discrete form the interface is reconstructed onto the staggered grid as a set of segments which connect the intersections of the $d = 0$ level with the bilinear interpolation of the values the function d takes at the four nodes of the cell (Fig. 1). Although this choice implies that the interface reconstruction is only first order accurate in space, it provides the interface portion within one cell without involving the values the function d takes at the nodes of the contiguous cells, which makes the reconstruction procedure very straightforward even in presence of complex interface topologies.

In order to keep the width of the jump region separating the two fluids constant through time, the function d is reinitialized by computing the minimum distance from the new interface configuration to the cell centers. It is worth remarking that, to avoid changing the interface location throughout the reconstruction process, the distance function is not reinitialized at the nodes belonging to cells crossed by the interface [25].

In the following, results provided by a coarse and a fine grid are presented in order to evaluate the dependence of the solution on the discretization.

2.3. Initialization of the velocity field from the potential flow solution

The most peculiar aspect of the computational procedure lies in the coupling strategy adopted to initialize the two-fluids Navier–Stokes solver starting from the potential flow solution. The latter is provided in terms of free surface shape, with the corresponding distributions of velocity potential and its normal derivative along it. Starting from the above data, the initialization of the velocity field for the Navier–Stokes solver is done in the following steps:

1. interpolate and reinitialize the potential flow solution onto a finer discretization, with segment length comparable to the size of the cells used in the two-fluids approach;
2. solve the boundary value problem for the new discretization and derive the normal derivative of the velocity potential on the free surface;

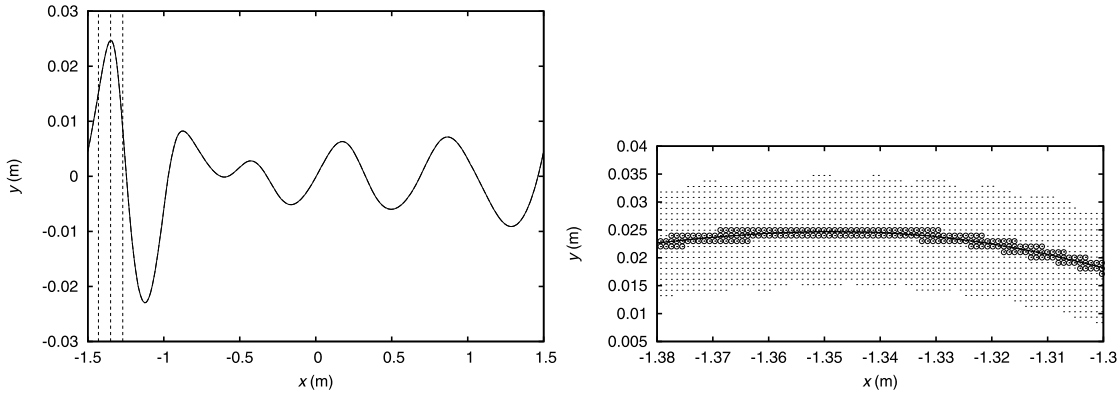

Fig. 2. On left, the free surface profiles of the original (*solid*) and interpolated (*dashed*) PFM solutions used to initialize the NS computation for the case with $\epsilon_0 = 0.12$. Note that the two solutions are overlapped and cannot be distinguished. The vertical dashed lines are those used to establish the comparisons presented in Fig. 3. Note that different scales are used for the vertical and horizontal axes. On right, a close up view of the steepest wave crest. In this case the same scale is adopted for the two axes. The grid points where the velocity is interpolated are indicated by dots and circles for the original and interpolated potential flow solutions, respectively.

3. initialize the Navier–Stokes grid;
4. use the boundary integral representation of the velocity potential to compute, by finite differences, the velocity field at the cell centers lying in the water domain;
5. formulate and solve the boundary value problem in the air domain imposing the continuity of the normal velocity at the interface;
6. compute the velocity field at the cell centers lying in the air domain using the boundary integral representation of the velocity potential in the air domain;
7. initialize the distance function;
8. smooth the velocity field about the interface.

The above points are discussed in detail below.

(1) As discussed at the end of Section 2.1, the potential flow solution is given in terms of a set of free surface segments with a piecewise constant distribution of the velocity potential and of its normal derivative. The use of the discretized solution into the boundary integral representation (5) provides accurate results only if the point $\boldsymbol{x}_P$ is far enough from the boundary. The width of the region where results are inaccurate depends on the order of the scheme: it is shown in the following that for the piecewise constant distribution, the solution is no longer reliable on points which are located at a distance from the interface smaller than the local panel size. In total, this implies that the velocity potential cannot be initialized in a layer about the interface twice the panel size thick.
In Section 3.1, it is shown that 60 panels per wavelength are enough for the potential flow simulations to get an accurate solution up to the breaking onset. This is not the case for the two-fluids solver which needs much finer discretizations in order to capture the breaking details. Simulations presented here use about 614 grid points per wavelength and a similar grid spacing is adopted in the vertical direction, at least about the still water level. Consequently, in order to reduce to the minimum the number of grid points where the velocity cannot be initialized accurately, it is necessary to derive a finer discretization of the potential flow solution to be used within the boundary integral representation (5). Of course, the increase in the number of free surface panels leads to an increase in the computational time needed to initialize the velocity field. Here the potential flow solution is interpolated and re-discretized with a size of the panels equal, or at least comparable, to the size of the grid cells. With this choice, moving in a direction orthogonal to the interface, there are only two, or at most three, grid points where the velocity is not computed directly from the boundary integral representation but is interpolated as discussed at point 8 of the procedure (see Fig. 2(b)).
The finer discretization is built by using a cubic spline with periodic conditions to interpolate the panel centroids ($\boldsymbol{x}_j^C$) of the original solution. The spline is parameterized using the distance measured along the polyline, which is $s_j^C = s_{j-1}^C + |\boldsymbol{x}_j^C - \boldsymbol{x}_{j-1}^C|$, with $s_1^C = 0$. Beside the centroids coordinates, the cubic spline is also used to interpolate the velocity potential using the parameter s_j^C for the interpolation.

(2) From the interpolated solution we only know the velocity potential and thus the boundary value problem, i.e. the boundary integral equation (7), has to be solved by using the new discretization in order to derive ϕ_n. At the end of the step we have a refined discretization of the potential flow solution which can be used in the boundary integral representation (5).

(3) The Navier–Stokes grid is initialized. For the problems under consideration, the grid is uniform in the horizontal direction whereas it is vertically clustered so as to have a region with uniform spacing about the still water level. The vertical spacing in this region is chosen so that $\Delta y = \Delta x$, Δx and Δy denoting the cell dimension. The vertical dimension of the cells grows moving upwards or downwards the free surface. Further details concerning the grid adopted in the numerical simulations are provided in Section 3.1.

(4) The velocity field is initialized at the cell centers belonging to the water domain. For the initialization of the velocity components at the grid point with coordinates (x, y) the velocity potential is computed at four points located at $(x \pm \Delta x/5)$ and $(y \pm \Delta y/5)$. The two velocity components $u = \partial\phi/\partial x$ and $v = \partial\phi/\partial y$ are derived by a second order finite difference scheme. The boundary integral representation (5) being valid only for points which are strictly inside the domain, the velocity at the point (x, y) is computed only if all the four points involved in the computation are inside the water domain. The check is done by a Point in Polygon algorithm similar to that described in [28].

(5) It is assumed that the air domain is bounded by the free surface below whereas the top boundary coincides with the top boundary of the computational domain chosen for the NS simulations. In order to initialize the velocity field in air, the velocity potential distribution is needed. To this purpose the boundary value problem (7) is formulated in terms of the velocity potential in air ϕ^a. At the side boundaries, where periodic conditions are enforced, the same technique discussed at the end of Section 2.1 for the water domain is adopted. The top boundary, located at $y = y_T$ $(y_T > 0)$ is accounted for by exploiting the image effect in the Green's function for the air domain, as done in Eq. (6), that is:

$$G^{*a}(\boldsymbol{x}_P - \boldsymbol{x}_Q) = \frac{1}{2\pi}\left[\log\left(|\boldsymbol{x}_P - \boldsymbol{x}_Q|\right) + \log\left(|\boldsymbol{x}_P - \boldsymbol{x}_Q^{*a}|\right)\right], \tag{15}$$

where $\boldsymbol{x}_Q = (x_Q, y_Q)$ and $\boldsymbol{x}_Q^{*a} = (x_Q, 2y_T - y_Q)$.
The most relevant difference concerns the boundary condition at the free surface. Differently from the water domain, where a Dirichlet condition is enforced by integrating the Bernoulli's equation in time, for the air side the continuity of the normal velocity at the interface is enforced. Hence, the boundary integral equation (7) is solved by using the interpolated solution derived at point 1 of this procedure, along with the Neumann condition $\phi_n^a = -\phi_n$ enforced at the free surface, where ϕ_n is the normal derivative of the velocity potential in water, as computed at point 2. The difference in the sign is due to the different orientation of the normals which are oriented inwards the domains. The solution of the boundary integral equation provides the velocity potential at the free surface, which can be used in the boundary integral representation (5) to derive velocity potential in the air domain and thus to initialize the velocity field.

(6) The velocity field in air is initialized by following the same procedure adopted for the water domain (point 4 of the procedure).

(7) The interpolated free surface shape is also used for the initialization of the distance function d which is needed by the two-fluids model for the initialization of the density distribution. This is done by taking, at each grid node, the minimum distance from each free surface segments. The sign of the distance is assigned as positive or negative depending if the grid node is in water on in air, respectively. The distinction is again made by using the Point in Polygon algorithm.

(8) The velocity field provided by this procedure has a jump in the tangential velocity component across the interface. Whereas such a discontinuity is consistent with the potential flow assumption and the zero stress condition at the interface, it is not consistent with the assumptions done in the two-fluids approach. In the latter, the momentum equation is discretized across the interface and thus the finite difference scheme smooth the jump at the very first step. Furthermore, in the two-fluids model a variable density and viscosity, appear in the momentum equation. As shown in [29], the jump in the tangential velocity is suddenly smoothed out over a region which is comparable to that used for to smooth the jump in the fluid properties. Due to the density and viscosity variation, some spurious components occur which make the velocity field inside that layer not completely meaningful. It is worth noticing that since the density distribution is reinitialized at each step, those components remain confined within the layer and do not affect the solution outside [25].
As discussed in Section 2.2, such a layer is usually five to ten cells thick. Hence, when interpolating the solution, we found unnecessary, albeit practically feasible but for grid points located just at the interface, to refine the discretization of the potential flow solution up to have an accurate velocity reconstruction at all the grid points. Instead, we left the velocity not initialized at a few grid points, up to a maximum of three, about the interface (Fig. 2). The velocity at those points is assigned by a linear interpolation of those at the two grid points lying at the same horizontal position but located next to the non-initialized region. More details on the effects of the smoothing of the initial velocity distribution are provided in [30].

In order to prove the effectiveness of the interpolation procedure, in Fig. 2 the free surface profiles before and after interpolation are shown along with the set of grid points which are considered as inaccurate for the two different discretizations. The differences in the free surface profile are not distinguishable, but the different panel length is made evident by the different width of the region which is excluded by the computation when using the original and interpolated discretizations. In Fig. 3 the vertical profiles of the horizontal and velocity components obtained from the original and interpolated discretizations are shown at three different positions about the crest of the steepest wave. For the sake of the clarity, the profiles in air and water are drawn in different figures. In all cases the profiles provided by the original and interpolated solutions are

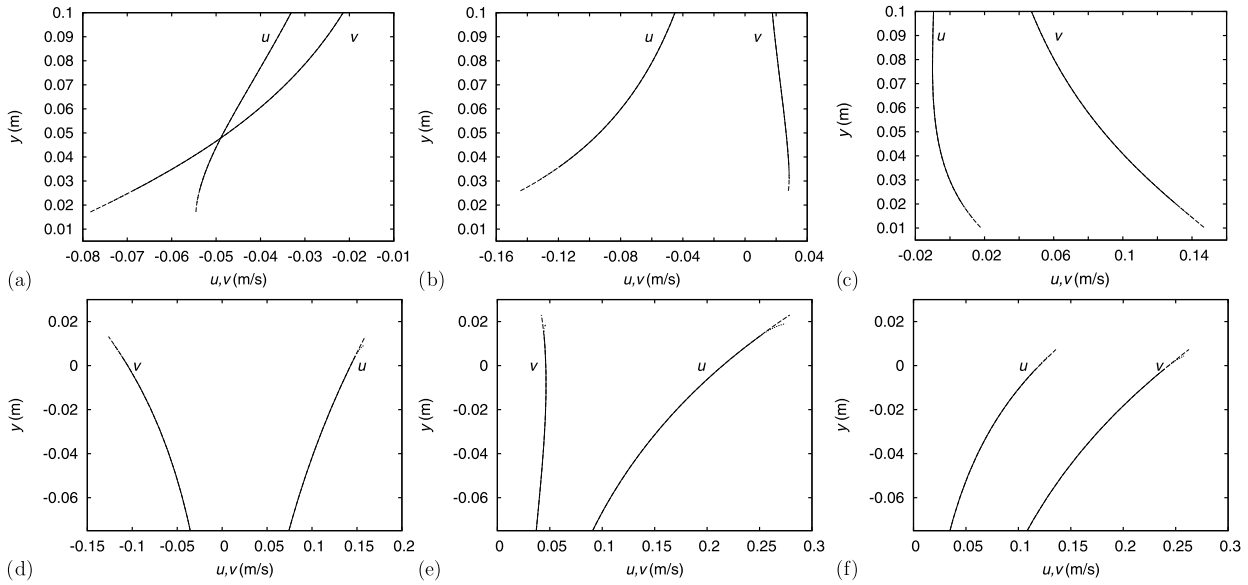

Fig. 3. Vertical profiles of the u and v velocity components in air (*top row*) and water (*bottom row*). The profiles are drawn at three positions about the wave crest as indicated in Fig. 2(a). For each profile, three solutions are drawn: the velocity computed by the original discretization up to a distance equal to the panel size (*solid*), the velocity computed by the interpolated discretization up to a distance equal to the panel size (*long dashes*), the velocity computed by the original discretization up to a distance equal to half the panel size (*short dashes*).

essentially overlapped which supports the choice of one panel amplitude as limit distance from the interface for the use of the boundary integral representation in discrete form. This is further confirmed by looking at the velocity profiles derived by the original discretization up to half the panel size. At least in some of the cases, at distances smaller than the panel size the profiles start to deviate from those provided by the interpolated solution.

3. Applications to a modulational instability case

3.1. Case study

The computational approach described in the previous section is used to study the evolution of modulated wave trains for different values of the initial wave steepness. At $t = 0$ a modulated wave train is initialized as a potential flow solution as follows:

$$\begin{aligned}\phi(x, y, 0) = {} & A_0\sqrt{g/k_0}\exp(k_0 y)\sin(k_0 x) \\ & + A_1\sqrt{g/k^+}\exp\left(k^+ y\right)\sin\left(k^+ x\right) \\ & + A_1\sqrt{g/k^-}\exp\left(k^- y\right)\sin\left(k^- x\right),\end{aligned} \tag{16}$$

where k_0 is the wavenumber of the fundamental component. Within the linear water wave assumption, the solution given in Eq. (16) corresponds to a free surface elevation $\eta(x, t)$ given by

$$\eta(x, 0) = A_0\cos(k_0 x) + A_1\cos\left(k^+ x\right) + A_1\cos\left(k^- x\right). \tag{17}$$

The amplitude of the fundamental component A_0 is expressed in terms of the initial steepness ϵ_0 as $A_0 = \epsilon_0/k_0$. In the following, simulations are presented for ϵ_0 in the range 0.10 to 0.18, step 0.02. The wavenumbers of the sideband perturbations are related to the fundamental wavenumber by the relation $k^{\pm} = k_0 \pm \Delta k$ with $\Delta k = k_0/5$ and their amplitude is $A_1 = 0.1A_0$. The conditions are the same used in [31] for $N = 5$ and a phase angle $\theta = 0$. Similar studies have been carried out in [11] and [32].

Simulations presented in the following refer to a fundamental component $\lambda_0 = 0.60$ m, with $g = 9.81\ \mathrm{m\,s^{-2}}$. According to linear theory, the fundamental component is characterized by a period $T = \sqrt{2\pi\lambda/g} \simeq 0.62$ s. In the two-fluids modeling fluid properties are the standard ones, i.e. $\varrho_a = 1.25\ \mathrm{kg\,m^{-3}}$ and $\varrho_w = 1000\ \mathrm{kg\,m^{-3}}$ for the densities and $\mu_a = 1.8 \times 10^{-5}\ \mathrm{kg\,m^{-1}\,s^{-1}}$ and $\mu_w = 10^{-3}\ \mathrm{kg\,m^{-1}\,s^{-1}}$ for the dynamic viscosity coefficients. In the Navier–Stokes simulations the surface tension coefficient is assumed as that in standard conditions for air and water, that is $\sigma = 0.073\ \mathrm{N\,m^{-1}}$.

In the following sections results are generally presented in dimensional form with the aim of facilitating their interpretation, although some results in non-dimensional form are also provided when needed to derive some more general conclusions.

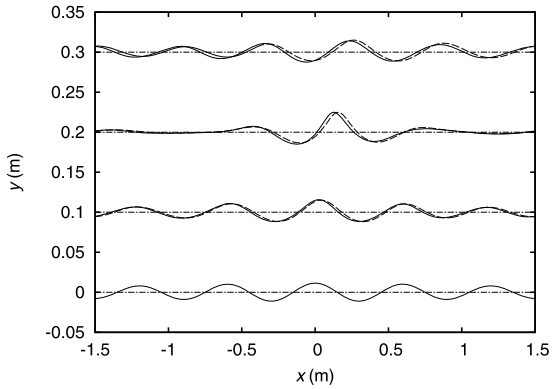

Fig. 4. Free surface profiles provided by the potential flow solution for the case $\epsilon_0 = 0.10$. The solid and dashed lines represent the fine and coarse grid computations, respectively. From bottom to top, the solutions refer to $t = 0, 35.75, 71.50, 107.25$ s. A vertical shift of 0.1 m is applied in order to distinguish the solutions at different times.

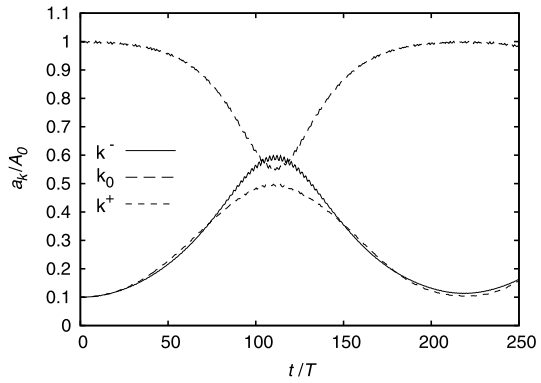

Fig. 5. Time histories of the wavenumber components provided by the potential flow computation for the case with $\epsilon_0 = 0.10$.

3.2. Fully non-linear potential flow simulations of the pre-breaking phase

Up to the breaking onset, the evolution of the modulated wave train can be simulated quite accurately and efficiently by the fully non-linear potential flow model (PFM). Simulations are performed by using a computational domain width of which, for the conditions adopted in this study, is five times the fundamental wavelength λ_0. For the discrete solution, 60 panels per fundamental wavelength are used. It is shown in [30] that this is enough to achieve an accurate description of the solution up to the onset of breaking. The bottom boundary is set at the same position as that used in the two-fluids Navier–Stokes simulations.

The case with $\epsilon_0 = 0.10$ is considered first. As shown in the sequence of Fig. 4, the nonlinear interaction between the different components leads to the formation of a wave much steeper than the initial one. However, if the initial steepness is not too large, even with the amplification factor associated to the modulational process, the maximum steepness remains below the threshold limit for the breaking occurrence. In the next stage, the wave system progressively returns back towards the original condition, as it is clearly evidenced by the time histories of the components at the three wavenumbers given in Fig. 5. The curves indicate that due to the modulational effect, the amplitude of the sideband components becomes comparable, or even larger, than that of the fundamental one. Beside the modulational effect, some components appear which are responsible for the oscillations in the amplitudes with a period which is twice the period T of the fundamental wave component. At least for this condition, the oscillations appear evident about the time at which the sideband components get the maximum amplitude. All the above results are essentially in line with what was already found by other authors, e.g. [9,11,12,31,32].

By increasing the steepness of the initial wave profile, the amplification factor associated to the modulational instability leads the steepness to exceed the threshold limit and the wave breaks. In Fig. 6 the solutions provided by the potential flow model at the time when the breaking starts, and the potential flow model stops, are shown for $\epsilon_0 = 0.12, 0.14, 0.16$ and 0.18, along with the corresponding solutions at the earlier time which are used to start the NS computation. The results show that the development of the instability and the onset of the breaking occur earlier for larger values of the initial steepness (Fig. 10). Although the behavior is about the same observed for $\epsilon_0 = 0.10$, the solution obtained for $\epsilon_0 = 0.12$ indicates that the component at k^- largely exceed the component at k_0. Moreover, for larger values of the initial steepness, the breaking starts before the maxima and minima of the wavenumber components are reached.

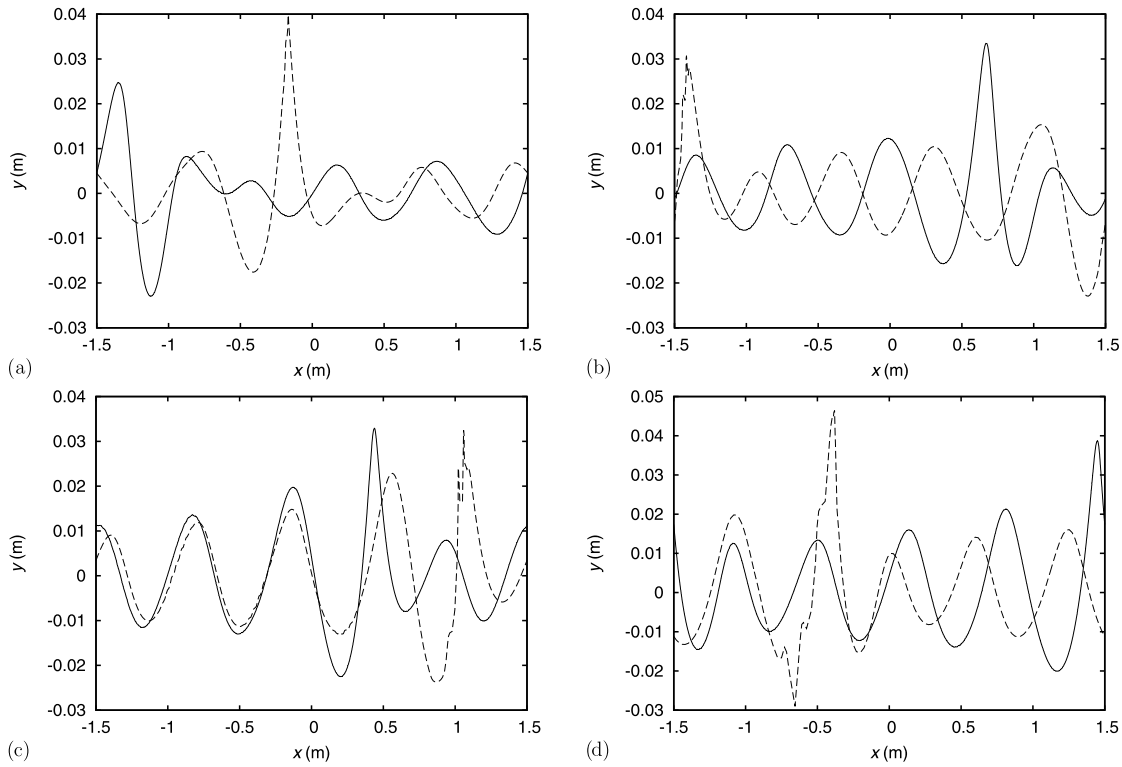

Fig. 6. Interface profiles at the time when the NS computation is started (*solid line*) and the last free surface configuration obtained by the potential flow solver (*dashed line*). Solutions refer to $\epsilon_0 = 0.12$ (a), 0.14 (b), 0.16 (c) and 0.18 (d).

With the potential flow model adopted in this study the breaking occurrence appears as a sudden instability of the integration in time. As discussed in the previous section, the potential flow solution obtained a few time instants before the onset of the breaking is used to initialize the velocity fields in air and water and to start the two-fluids simulations.

3.3. Two-fluids numerical simulations of the breaking processes

The Navier–Stokes (NS) simulations are carried out on a computational domain which spans horizontally from $x = -1.5$ m to $x = 1.5$ m and vertically from $y = -2$ m up to 0.6 m above the still water level. A uniform discretization is adopted in the horizontal direction with $\Delta x = 1/512$ m and $1/1024$ m for the coarse and fine grids, respectively. In the vertical direction the grid is clustered about the still water level in order to achieve an accurate description of the breaking region. The vertical grid spacing is uniform, and equal to Δx, in the region from $y = -0.15$ to 0.15 m whereas it grows geometrically by a factor $\alpha = 1.03$ towards the top and bottom boundaries. This gives a total of 1536×336 and 3072×672 grid cells for the coarse and fine grids, respectively. The width of transition region 2δ is 0.02 m and 0.01 m for the two grids in order to have the density jump spread across about 10 grid cells for both grids. No slip boundary conditions are assigned at the top and bottom boundaries.

For the case at $\epsilon_0 = 0.12$ the PFM computation becomes unstable and stops at $t = 40.30$ s, thus indicating occurrence of the first breaking event at that time. The fundamental period being $T \simeq 0.62$ s, that corresponds to about 65 wave periods from the initial start. The NS simulation is started from the PFM solution at $t = 39.70$ s. The comparison between the PFM and the NS solutions at $t = 40.00$ s shows that the interface profiles are essentially overlapped each other, aside from a region about the crest of the breaking wave where the NS solution exhibits a sharper curvature in the fore part and a flatter crest (Fig. 7(top)).

As the solution advances in time, the wave breaks. The NS solution displays the formation of a tiny jet propagating forward, while the wave is still steepening. The thinnest part of the jet is fragmented into drops before plunging onto the free surface ahead, partly due to the limits in the grid discretization and to the finite thickness adopted for the transition region (Fig. 8). In the figure the interface profiles provided by the coarse and fine grid computations are depicted, exhibiting a rather satisfactory agreement, although the coarse grid computation misses some of the finest details. It is worth remarking that the coarse grid, besides larger grid cells, is also characterized by a wider transition region, which is the reason why the jet tip is filtered out.

The interaction between the different wavenumber components causes a reduction of the steepness which in turn leads to an interruption of the breaking process. The modulation of the steepness is recurrent with a period associated to the

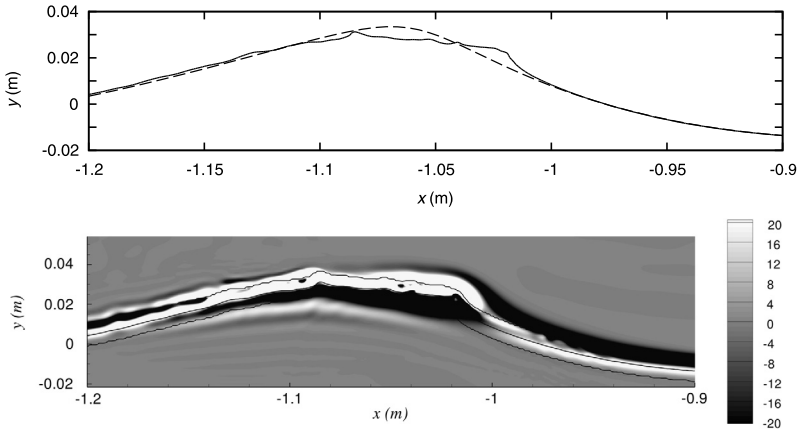

Fig. 7. On top, the free surface profiles provided by the PFM (*dashed*) and NS (*solid*) for the case at $\epsilon_0 = 0.12$ shortly after the start of the NS computation are shown. On bottom, the vorticity distribution about the wave crest is shown for the NS solution. The legend for the vorticity distribution is provided on the right in s^{-1} units. From this contours it can be seen that, at least in the early stage, the breaking is of the spilling type, with the formation of a bulge with a sharp curvature at the toe and a separation of the flow in water to separate, which leads to a shear layer beneath the crest [14]. Correspondingly, a flow separation takes place also in air.

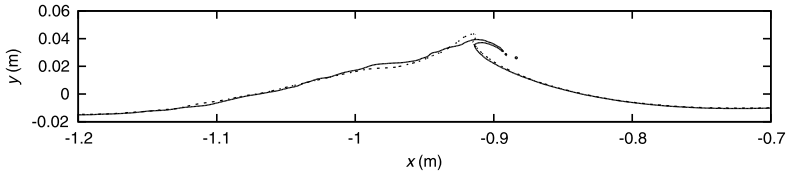

Fig. 8. Comparison between the free surface profiles obtained by two-fluids simulation with the coarse (*dashed line*) and fine (*solid line*) discretizations at the onset of the first breaking event for the case $\epsilon_0 = 0.12$.

group velocity, and thus a new steepening process and a new breaking event occur about $2T$ after the first event. The recurrence of the breaking process is highlighted in Fig. 9(a) where a quite long sequence of the free surface profiles for the case with $\epsilon_0 = 0.12$ is drawn. A vertical displacement equal to the corresponding time is applied at each profile and the free surface elevation is multiplied by a factor 5 in order to make the profiles clearer. The recurrence of the breaking process, which is somewhat related to the oscillating components discussed in Section 3.2, is consistent with the experimental observations according to which the time interval between two successive breaking events T_b is about twice the fundamental wave period, i.e. $T_b \simeq 2T$ [9,33,34]. For the conditions adopted here $T_b \simeq 1.24$ s. Substantially similar results are obtained for steeper cases, as it can be seen from Fig. 9(b), which refers to the case with $\epsilon_0 = 0.18$.

In Fig. 10 the time histories of the three wavenumber components are drawn for the four breaking conditions. Both the PFM and the NS solutions are drawn, and the vertical line indicates the time at which the NS solution is started. As the NS solver is started before the breaking starts, there is an interval of time in which both the PFM and the NS solutions are available. This is clear in Fig. 10(d) where the interval of overlapping is about 2 s. The comparison between the three components provided by the two approaches is quite satisfactory, taking into account the different physical models adopted in the two approaches.

The results discussed so far are based on the free surface profiles only. A deeper understanding of the breaking process can be achieved by looking at the flow induced in air and water which is the topic of the next section.

3.4. Flow induced by the breaking process

Depending on the steepness reached at the onset, the breaking can be either plunging, with the ejection of a jet and with air entrainment, or a more gentle spilling, with very limited air entrainment [14]. Two examples are given in Fig. 11, where sequences of the velocity and vorticity distributions are provided for the two cases. In order to show the width of the transition region, the density line at the pure water value is also drawn. It has to be observed that due to the limits in the grid resolution, some of the finest details and the smaller drops/bubbles are not captured. Those aspects have been deeply investigated in previous studies, e.g. [8,14]. It is worth noticing that in the case of modulational instability the breaking starts soon after the threshold limit in the steepness is overtaken. As a consequence, the resulting breaking is not expected to generate large plunging jets as those observed nearshore. Because of the modulational process, the typology of the breaking can change during the event or from one event to the next. This can be seen by comparing the free surface profiles given in Fig. 7(top) and Fig. 8. They refer to the same condition and to the same breaking event. From the free surface profiles and vorticity contours given in Fig. 7 it is seen that the breaking starts as a spilling type, with the bulge

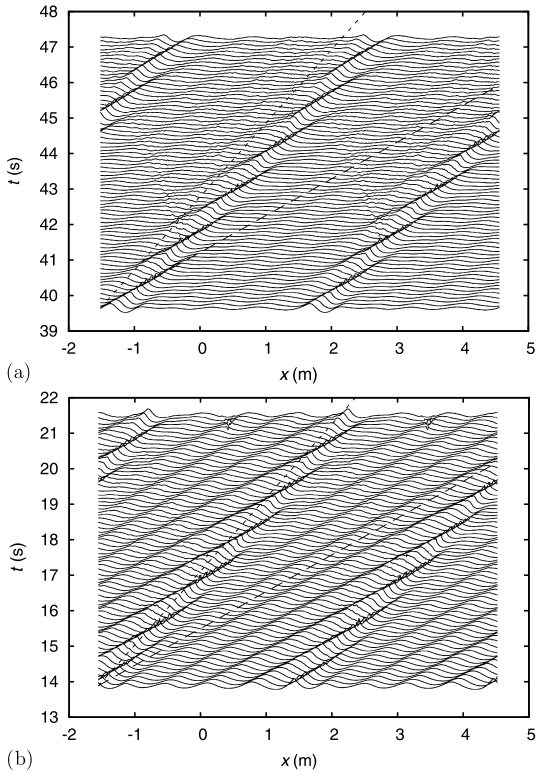

Fig. 9. Sequence of the free surface profiles obtained by the NS simulation for the case with $\epsilon_0 = 0.12$ (a) and $\epsilon_0 = 0.18$ (b). The time interval between two successive profiles is 0.1 s. The free surface elevation is amplified by a factor five in order to improve the readability. The group and phase lines are drawn in short and long dashes, respectively.

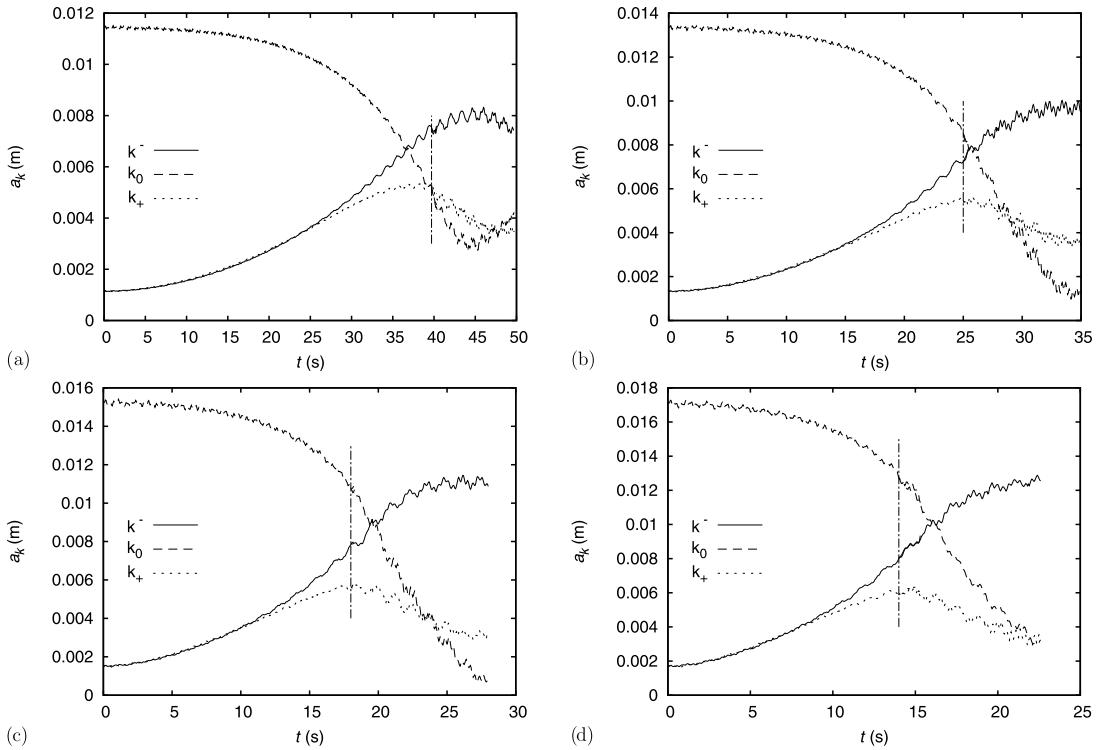

Fig. 10. Time histories of the wavenumber components. The vertical lines represent the time at which the NS simulations are started. Solutions refer to $\epsilon_0 = 0.12$ (a), 0.14 (b), 0.16 (c) and 0.18 (d).

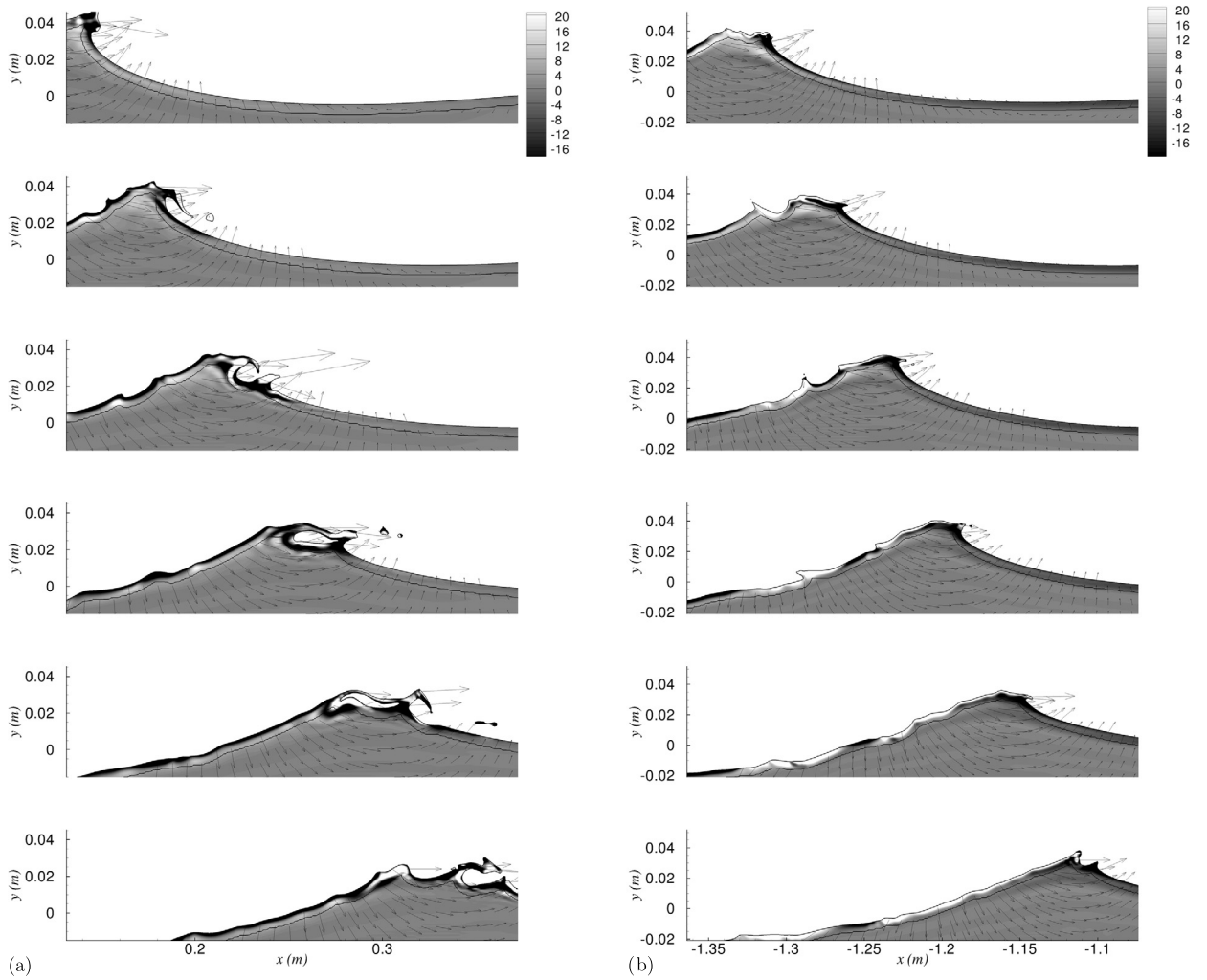

Fig. 11. Velocity and vorticity distributions for two different breaking events. The legend for the vorticity distribution, given in s^{-1} units, is provided on the top-right corner of each sequence. Velocity vectors are shown every eighth grid point for the sake of the clarity. The solid line beneath the free surface represents the pure water density limit. The two solutions refer to an intensive plunging breaking with air entrainment (a) and to a more gentle breaking event with no air entrained, up to the scales resolved by the model (b).

formed about the crest. The flow separation at the toe makes the crest flatter with respect to the PFM solution at the same time. However, in parallel to the formation of the bulge, the interaction between the different components of the wave system causes a further increase in the wave steepness and thus the breaking turns into a plunging type (Fig. 8).

Whereas the analysis of the velocity field induced in water by the breaking occurrence has been widely investigated in the past, e.g. [35–37], only a little is available on the air side, e.g. [14,23,38,39]. Often, the air side gets more interest in wind–wave interaction problems, e.g. [40,41]. Looking at the velocity and vorticity fields in the case of modulated wave trains, it is found that the occurrence of breaking causes the airflow to separate at the wave crest, leading to the formation of a large vortical structure. The interaction of this vortical structure with the free surface on the back of the wave generates a secondary vorticity structure of opposite sign which is eventually detached from the water surface. Experimental evidence of this phenomenon is shown in [42], although the conditions are different from those considered in this study. The interaction between the primary and secondary vorticity structures gives rise to a dipole which move under the self-induced velocity.

A sequence showing the formation of the primary and secondary vorticity structures and the detachment of the dipole is given in Fig. 12. Due to the recurrence in the breaking process, several dipoles are released in the air side which propagate upwards and arrive at a height which is comparable to about half the fundamental wavelength. A rather interesting aspect is that the general features of the airflow and vorticity intensity of the dipoles, seem not much dependent on the initial steepness, as long as breaking occurs. Differences are mainly in the height reached by the structures (Fig. 13).

The capabilities of the numerical model in describing the vorticity–free-surface interaction were carefully analyzed and validated versus a single phase model in [25]. Therein it was found that the model yields an accurate prediction of the secondary vorticity production, provided a sufficiently large number of cells is included in the transition region. In this

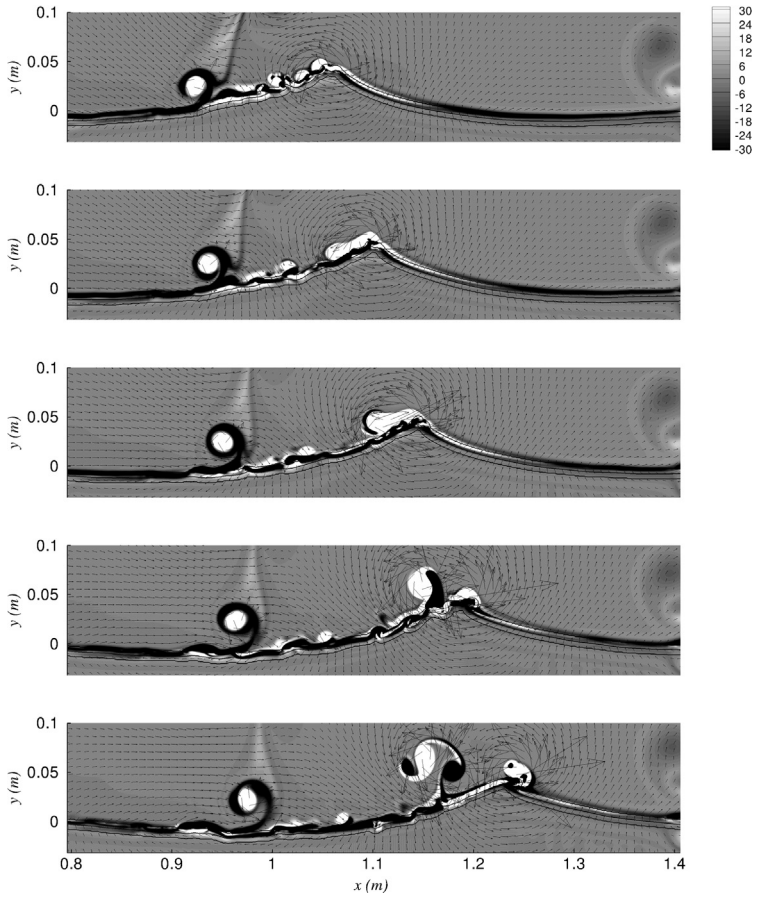

Fig. 12. Velocity and vorticity distributions during the airflow separation at the breaking crest. Velocity vectors are shown every eighth grid point whereas the legend for the vorticity distribution, given in s^{-1} units, is provided on the top-right corner of the sequence. The primary vortex structure interacts with the free surface leading to the formation of a secondary structure and eventually to a dipole which moves upwards due to the self-induced velocity. The solution here refer to the case with initial steepness $\epsilon_0 = 0.12$, but similar results are obtained for larger steepnesses, as shown in Fig. 13.

sense, it is believed that the vortical structures and their dynamics are scarcely dependent on the details of the initial conditions and on the use of a smooth density distribution.

The important role played by the breaking on the airflow can be inferred by looking at the NS solution for the case at $\epsilon = 0.10$, given in Fig. 14. For this condition the PFM does not predict breaking. Hence, the NS simulation is started at a time when the modulation gets close to the maximum. Simulations have been performed starting from different time instants and non-breaking solutions have been found in all cases. Soon after the NS computations start, a small amount of vorticity is shed in air, which is mainly related to the initial conditions and to the change in the physical model. However, the vorticity production ceases soon, even in presence of several steepening events. The fact that the vorticity production and the dipolar structures show only in presence of breaking confirms the important role played by the breaking on the flow in the lower atmosphere layer. From the numerical viewpoint, this indicates that initial conditions affect the solution only during a short initial transient period.

3.5. Energy dissipation

As discussed in the introduction, an important motivation for the study is the need of achieving an estimate of the energy dissipation associated to the breaking events induced by the modulational instability. The NS model providing a highly detailed description of the flow, helps in answering many of the open questions. There are however some limitations related to the smearing across a finite region of the density and viscosity jumps and of the surface tension effects [8].

On the basis of the density distribution assigned by Eq. (13), the kinetic and potential energy contents in water per unit of transversal length can be evaluated as follows

$$E_K^w(t) = \frac{1}{2} \int\limits_{d \geqslant 0} \varrho\left(u^2 + v^2\right) \mathrm{d}x\, \mathrm{d}y, \tag{18}$$

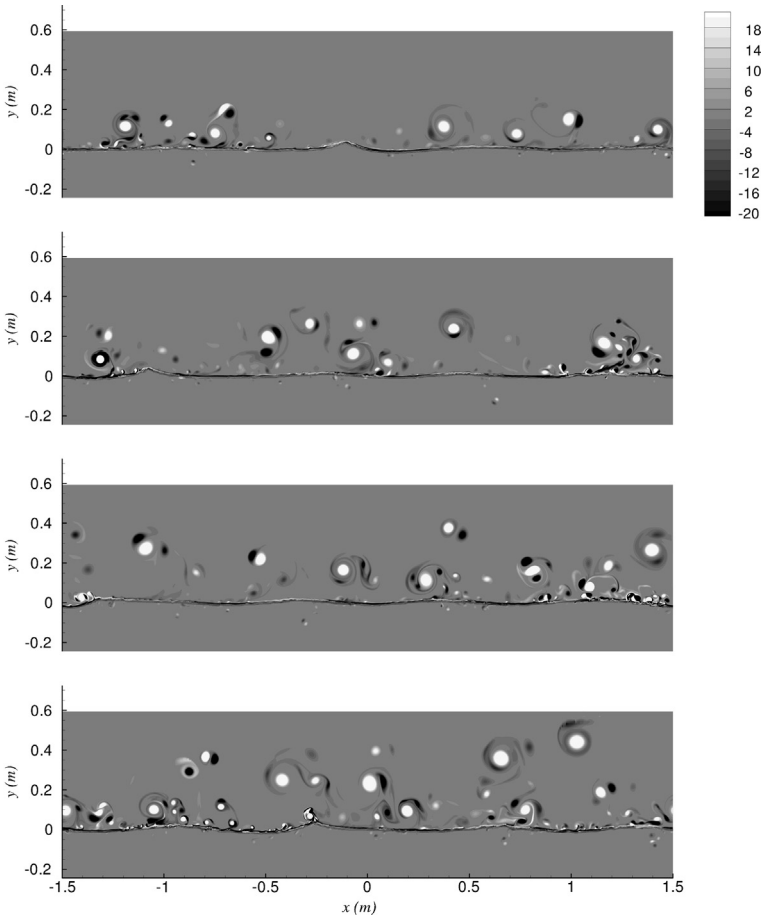

Fig. 13. Vorticity contours displaying the dipolar structures generated by the breaking process for different values of the initial steepness: from top to bottom $\epsilon_0 = 0.12, 0.14, 0.16, 0.18$. The contour legend of the vorticity, in s^{-1}, is given on top right. The three solid lines, very close to each other, represent the density contours at ρ_w, $(\rho_w + \rho_a)/2$, ρ_a so that the whole transition region can be identified.

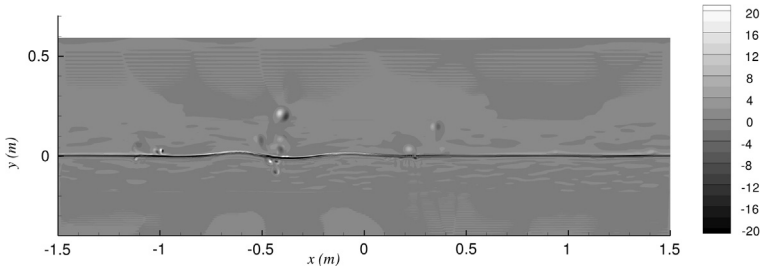

Fig. 14. Vorticity contour for the case with $\epsilon = 0.10$. The contour legend is in s^{-1}. In this case, a small amount of vorticity is released at the beginning of the simulation. Afterwards, without breaking, the airflow remains attached.

$$E_P^w(t) = \int_{d \geqslant 0} \varrho g y \, \mathrm{d}x \, \mathrm{d}y - E_P^{w0}, \tag{19}$$

where

$$E_P^{w0} = -\varrho_w g \frac{y_B^2}{2} L + O\left(\delta^2\right) \tag{20}$$

is the potential energy associated to the still water condition and L the width of the computational domain [14]. Similar equations hold for the air side, which are

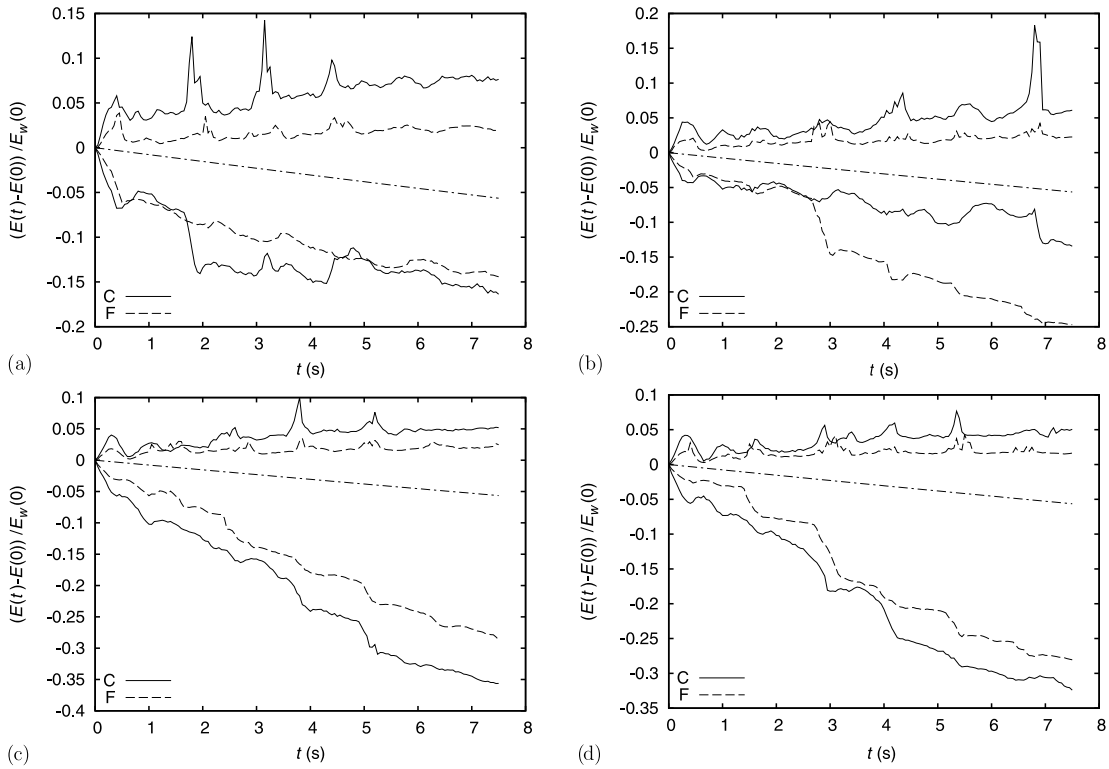

Fig. 15. Time histories of the energy content in water and air for the four simulations: $\epsilon_0 = 0.12$ (a), 0.14 (b), 0.16 (c) and 0.18 (d). The energy contents in water and air are in the negative and positive parts of the graph, respectively. The dashed lines refer to the fine grid computations, whereas the coarse grid results are drawn with solid lines. The dashed–dotted line is the decay law of the energy in water, as derived by the experimental measurements in [15]. The initial energy content in water and air have been subtracted, and the variation is made non-dimensional by the initial energy content in water. Note that the origin of the time axis is set to the time at which the NS simulations are started.

$$E_K^a(t) = \frac{1}{2}\int\limits_{d<0} \varrho\left(u^2+v^2\right)\mathrm{d}x\,\mathrm{d}y, \tag{21}$$

$$E_P^a(t) = \int\limits_{d<0} \varrho g y\,\mathrm{d}x\,\mathrm{d}y - E_P^{a0}, \tag{22}$$

where

$$E_P^{a0} = \varrho_a g \frac{y_T^2}{2} L + O\left(\delta^2\right) \tag{23}$$

y^T being the coordinate of the top boundary. The total energy content is evaluated as the sum of the kinetic and potential energy contributions.

It is worth noticing that the above equations refer to the nominal air and water domains, which are the ones identified by the interface. But in those domains the density is not constant and some spurious components in the velocity field appear for $|d| < \delta$, which may have influence on the kinetic energy as well.

The time histories of the total energy contents in air and water for the four different cases are drawn in Fig. 15. In order to highlight the variations, the initial energy contents have been subtracted and the variation are made non-dimensional by the initial energy content in water. Results obtained by the coarse and fine discretizations are drawn with the purpose of estimating the grid dependence of the solution. As soon as the NS simulations start, an energy fraction ranging between 3 to 7% of the initial energy content in water is transferred from water to air. This is a consequence of the redistribution of the velocity field inside the transition layer which occurs to make it consistent with the smooth density variation used in the two fluids approach. The energy fraction is smaller in the fine grid computations due to the narrower transition region with respect to the coarse grid case. The results display spikes in the energy content in air concurrent with the breaking events. Such energy transfer is mainly due to the normal stresses occurring at the interface in consequence of the separation of the air flow at the breaking crest. Correspondingly, sharp drops characterize the energy content in water. The energy reduction is bigger for larger ϵ_0, due to the stronger breaking. As already noted, the breaking is recurrent with a period $T_b \simeq 1.24$ s, which is about the period at which the sharp energy variations take place.

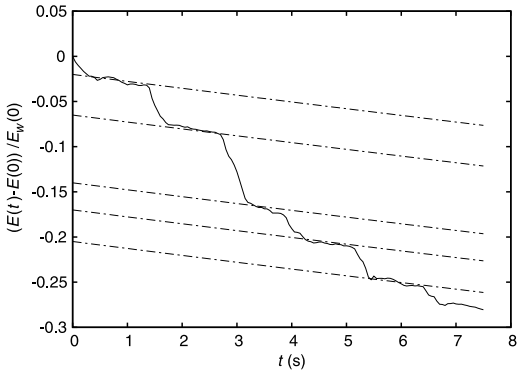

Fig. 16. Time histories of the energy content in water for the case $\epsilon_0 = 0.18$. The steps indicate the energy amount dissipated at each breaking event, whereas between two events the energy decay follows quite nicely the decay rate measured in [15] (*dash-dotted*).

The comparisons between the results provided by the two grids are generally in a satisfactory agreement, and it improves for larger ϵ_0. This is due to the larger structures formed in those cases, which are well captured by both the fine and coarse grids. For the cases with lower ϵ_0 the breaker is small and some of the finest details are not properly captured by the coarse grid computation because of the wider transition region. Aside from the different capabilities of the two grids in resolving the finest details of the flow about the interface, such as tiny drops or bubbles, the different thickness of the transition region leads to different density distributions with corresponding differences in the spurious velocity field, both entering into the evaluation of the energy contents by Eqs. (18), (22). Such limitations could be overcome by adopting sharp interface approaches, like the ones proposed by [22] or [43] or by [39].

Another important effect which has to be considered when comparing different simulations, is the uncertainty in the numerical solutions in the case of wave breaking flows. Due to the strong nonlinearity of the free surface flow in presence of wave breaking processes, even minor perturbations to the solution, or minor differences in the initial conditions or in the grid details, may generate large differences in both local and global quantities. This point is analyzed and discussed in depth in [8], where estimates of the uncertainty of some global quantities are also provided.

Besides the energy drops associated to the breaking events, the wave propagation is affected by other dissipation terms. The dissipation characterizing modulated wave trains of about comparable wavelengths has been measured by [15] at the early stage of the modulational process. The energy variation is presented in the form

$$E(x) = E(0)\exp(-2\sigma_e x) \tag{24}$$

where the coefficient σ_e is found to be in the range (0.0056–0.0072) m^{-1}. On the basis of some theoretical arguments, they estimated that the dissipation due viscous effects at the wall would give a decay coefficient of about 0.0028 m^{-1}, much lower than the measured one.

In order to establish a comparison with the experimental decay rate, the effect of the walls, which are not present in our configuration, are subtracted by the measured coefficient and a decay coefficient $\sigma_d = 0.0040$ m^{-1} is used for comparison. Eq. (24) is transformed in a time depending function by using the phase velocity, $x = c_p t$, where $c_p = (g\lambda/2\pi)^{1/2}$. Hence, the energy dissipation is expressed as

$$E_m(t)/E_m(0) = \exp(-2\sigma_d c_p t). \tag{25}$$

The line representing the measured dissipation rate is reported in Fig. 15 in dash-dotted line. It can be seen that between two successive breaking events, the numerical results follows very well the measured dissipation rate. This is clearer for the simulations with larger ϵ_0 because of the larger energy drop characterizing the breaking events. For the case with $\epsilon_0 = 0.18$ the agreement between the measured dissipation rate and the numerical results is made evident in Fig. 16 where the decay rate given by Eq. (25) is drawn between two successive breaking events. The vertical distance between the two lines represents the energy fraction dissipated by each single breaking event, which represent 3 to 7% of the initial energy content.

Some additional comments are needed with respect to the dissipation associated to the non-breaking propagation. According to the previous considerations, even before the breaking occurrence, there is a dissipation term which may have some effects on the growth rates of the sideband components [15]. Such dissipation term is not included in the PFM simulation, and that needs to be justified.

It is said in the introduction that the final aim of the study is to derive a parameterization of the breaking phenomenon which can be used in computational models commonly employed to describe the wave dynamics on large scales, which are generally based on spectral approaches. Hence, we should arrive at a relation between the pre-breaking spectrum, the energy dissipation associated with the breaking process and the post-breaking spectrum. It is assumed that the dissipated energy fraction and the modification to the spectrum, depends only on the pre-breaking spectrum but not to the way the

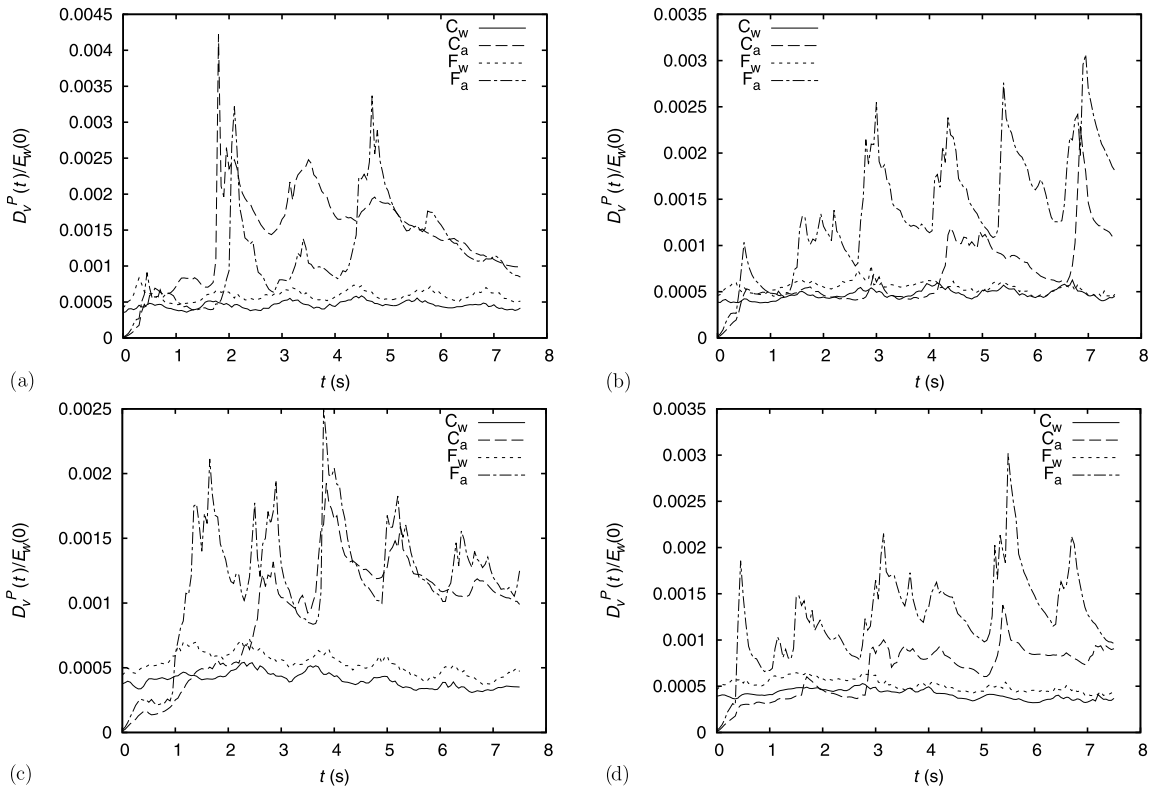

Fig. 17. Time histories of the viscous dissipation in pure air and pure water domains, as defined by Eqs. (27) and (26). Solutions are given for $\epsilon_0 = 0.12$ (a), 0.14 (b), 0.16 (c) and 0.18 (d). Results indicate that the viscous dissipation level in air is generally larger than that in water and is strongly enhanced during the breaking occurrence. In the keys C and F are used to denote coarse and fine grid results, respectively.

wave system arrived at that condition. The results should be the same for a wave system propagating without dissipation and for a steeper wave system propagating with some dissipation, provided the pre-breaking spectrum is the same. The present work is focused on the breaking phase and on the physical phenomena involved in it but not much on the wave dynamics before the breaking. It is assumed that the wave forecasting approaches commonly employed, properly account for the dissipation of non-breaking wave propagation already.

The detailed description of the velocity field and of the air water domains, in principle allows to extract many information regarding the transfer of forces, momentum and energy between air and water. However, due to the spurious components already discussed, the evaluation of the fluxes is not reliable. The only contribution which can be estimated with a satisfactory level of confidence, aside from the uncertainty component, is the viscous dissipation term. Of course also in this case the spurious velocity component would enter the estimates. But the effect can be significantly reduced if, instead of integrating the viscous dissipation in the nominal domains, the integration is limited to regions where the density is constant, either pure air or pure water values.

The viscous dissipation in water and air per unit of transversal length, is then evaluated as

$$D_v^{Pw} = 2\mu_w \int\limits_{d>\delta} e_{ij} \frac{\partial u_i}{\partial x_j} \,\mathrm{d}x\,\mathrm{d}y, \tag{26}$$

$$D_v^{Pa} = 2\mu_a \int\limits_{d<-\delta} e_{ij} \frac{\partial u_i}{\partial x_j} \,\mathrm{d}x\,\mathrm{d}y, \tag{27}$$

respectively. In the above equations e_{ij} is the strain tensor, which is

$$e_{ij} = \frac{1}{2}\left(\frac{\partial u_i}{\partial x_j} + \frac{\partial u_j}{\partial x_i}\right).$$

Of course the use of Eqs. (26) and (27) implies that the estimates miss the contributions of the transition layer nearby the interface and, furthermore, they depends on the thickness of the transition region.

The curves representing the viscous dissipation in pure air and pure water are shown in Fig. 17. In order to make results comparable, the dissipation terms are scaled by the corresponding initial energy contents in water. The results display high

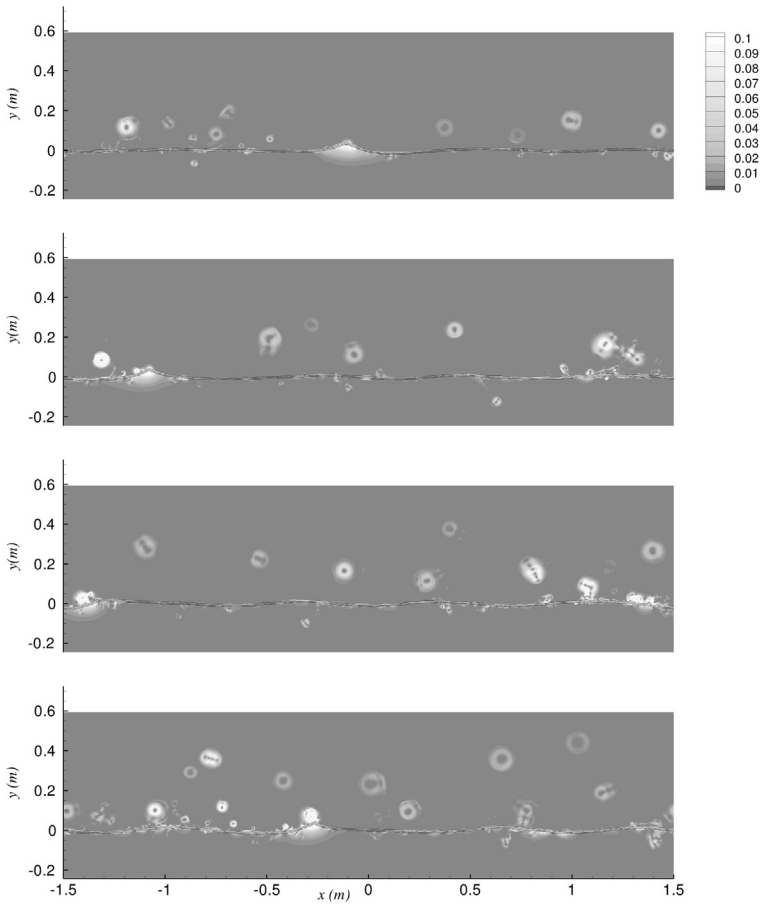

Fig. 18. Viscous dissipation contours in air and water, as defined by Eqs. (26), (27), showing that most of the viscous dissipation occurs in air. From top to bottom results refer to $\epsilon_0 = 0.12, 0.14, 0.16, 0.18$. The contour legend, in $\mathrm{kg\,m/s^2}$, is given on top right. The solid lines represent the density contours at ρ_w, $(\rho_w + \rho_a)/2$. The configurations are the same as that in Fig. 13.

level of viscous dissipation in air, concurrent with the breaking event. An increase in the dissipation level is found also in water, although it is generally much smaller.

By integrating the viscous dissipation terms in the two media, it can be shown that, for the time interval considered in this study, the total viscous dissipation in the pure air region can be up to three times the corresponding one in pure water [18].

The viscous dissipation contours for the four cases are given in Fig. 18. The important contribution provided by the dipole structures is clearly highlighted. Large dissipation levels are found within the transition region, which is bounded by the density lines in the figures, but they are very likely unphysical as affected by the spurious velocity components in the transition region.

4. Conclusions

In this paper a computational method for the study of the breaking process generated by modulational instability is presented. The method exploits the combination between a fully non-linear potential flow model and a two-fluids Navier–Stokes solver. The former is efficiently used to describe the dynamics of the wave system in the long initial transition during which the instability develops. Hence, the potential flow solution a few time instants before the onset of the breaking is used to initialize the velocity field in the air and water from which the two-fluids approach starts.

The method is applied to study the evolution to breaking of modulated wave trains with different values of the initial steepness. It is shown that the modulated wave train develops breaking if the initial steepness is larger than a threshold value. Differently from the breaking of a steep wave obtained by linear superposition, in the case of modulated wave trains each breaking event lasts a short interval of time but it restarts again in about two wave periods. The recurrence is expected to stop once sufficient energy is lost, but it is not yet clear how soon that happens.

The results in terms of the free surface profiles and wavenumber components display a good degree of regularity when passing from the potential flow model to the two-fluids computations. The analysis of the velocity and vorticity fields dis-

plays the formation of large dipole structures which propagate upwards to heights comparable to half the fundamental wavelength. It is shown that such vortical structures appear together with the breaking, whereas in the non-breaking case, only a little amount of vorticity is shed, which is mainly related to some artificial effects in the initial conditions. By analyzing the energy components, the energy dissipation associated to each breaking process is distinguished. Although a further and more detailed analysis of the results is needed, such information can answer the open questions which motivated the study. The analysis of the flow revealed high dissipation values in the air side. This may lead to underestimates of the dissipation term in laboratory estimates based on measurements of the velocity field in water only, e.g. [15].

There are several limitations with the two-fluid model. First of all, the two-dimensional assumption, which prevents an accurate description of the vorticity and interface dynamics. Also, the adopted resolution seems fine for the stronger breakings, whereas some details are missing for more gentle breaking events. The role played by the finest details on the solution has to be investigated further.

As a final consideration, it is worth noticing that the coupling procedure which has been developed here for the fully nonlinear potential flow approach can be extended, without any relevant modification, to work in combination with other methods more commonly adopted to study the wave dynamics on large scales provided they are formulated in terms of the velocity potential, e.g. [16]. This would make it simpler to explore the dependence of the breaking characteristics on the pre-breaking wave spectrum.

Acknowledgements

The work by A.I. was funded by the Flagship Project RITMARE, the Italian Research for the Sea, coordinated by the Italian National Research Council and funded by the Italian Ministry of Education, University and Research within the National Research Program 2011–2013. The work by M.O. was supported by ONR Grant No. 214 N000141010991 and by MIUR Grant PRIN 2012BFNWZ2.

References

[1] M. Perlin, W. Choi, Z. Tian, Breaking waves in deep and intermediate waters, Annu. Rev. Fluid Mech. 45 (2013) 115–145.
[2] A.V. Babanin, Breaking and Dissipation of Ocean Surface Waves, Cambridge University Press, 2011, 480 pp.
[3] L. Cavaleri, Wave modeling: Where to go in the future, Bull. Am. Meteorol. Soc. 87 (2006) 207–214.
[4] A.V. Babanin, D. Chalikov, I.R. Young, I. Savelyev, Predicting the breaking onset of surface water waves, Geophys. Res. Lett. 34 (2007) L07605.
[5] A. Toffoli, O. Gramstad, K. Trulsen, J. Monbaliu, E. Bitner-Gregersen, M. Onorato, Evolution of weakly nonlinear random directional waves: laboratory experiments and numerical simulations, J. Fluid Mech. 664 (2010) 313–336.
[6] A.V. Babanin, T. Waseda, T. Kinoshita, A. Toffoli, Wave breaking in directional fields, J. Phys. Oceanogr. 41 (2011) 145–156.
[7] R.J. Rapp, W.K. Melville, Laboratory measurements of deep-water breaking waves, Philos. Trans. R. Soc. A 331 (1990) 735–800.
[8] A. Iafrati, Numerical study of the effects of the breaking intensity on wave breaking flows, J. Fluid Mech. 622 (2009) 371–411.
[9] A.V. Babanin, D. Chalikov, I.R. Young, I. Savelyev, Numerical and laboratory investigation of breaking of steep two-dimensional waves in deep water, J. Fluid Mech. 644 (2010) 433–463.
[10] D. Chalikov, A.V. Babanin, Simulation of breaking in spectral environment, J. Phys. Oceanogr. 42 (2012) 1745–1761.
[11] M.P. Tulin, T. Waseda, Laboratory observation of wave group evolution, including breaking effects, J. Fluid Mech. 378 (1999) 197–232.
[12] M. Landrini, O. Oshri, T. Waseda, M.P. Tulin, Long time evolution of gravity wave system, in: Proc. 13th Int. Workshop Water Waves Floating Bodies, Alphen aan den Rijn, Netherlands, 1998, www.iwwwfb.org.
[13] D. Chalikov, D. Sheinin, Modeling extreme waves based on equations of potential flow with a free surface, J. Comput. Phys. 210 (2005) 247–273.
[14] A. Iafrati, Energy dissipation mechanisms in wave breaking processes: spilling and highly aerated plunging breaking events, J. Geophys. Res. 116 (2011) C07024.
[15] Y. Ma, G. Dong, M. Perlin, X. Ma, G. Wang, Experimental investigation on the evolution of the modulation instability with dissipation, J. Fluid Mech. 711 (2012) 101–121.
[16] W. Xiao, Y. Liu, G. Wu, D.K.P. Yue, Rogue wave occurrence and dynamics by direct simulations of nonlinear wave-field evolution, J. Fluid Mech. 720 (2013) 357–392.
[17] A.D. Drazen, W.K. Melville, L. Lenain, Inertial scaling of dissipation in unsteady breaking waves, J. Fluid Mech. 611 (2008) 307–332.
[18] A. Iafrati, A. Babanin, M. Onorato, Modulational instability, wave breaking, and formation of large-scale dipoles in the atmosphere, Phys. Rev. Lett. 110 (2013) 184504.
[19] M.S. Longuet-Higgins, E.D. Cokelet, The deformation of steep surface waves on water. I. A numerical method, Proc. R. Soc. A, Math. Phys. 350 (1976) 1–26.
[20] D. Battistin, A. Iafrati, Hydrodynamic loads during water entry of two-dimensional and axisymmetric bodies, J. Fluids Struct. 17 (2003) 643–664.
[21] D. Battistin, A. Iafrati, A numerical model for the jet flow generated by water impact, J. Eng. Math. 48 (2004) 353–374.
[22] J. Yang, F. Stern, Sharp interface immersed-boundary/level-set method for wave-body interactions, J. Comput. Phys. 228 (2009) 6590–6616.
[23] G. Chen, C. Kharif, S. Zaleski, J. Li, Two-dimensional Navier–Stokes simulation of breaking waves, Phys. Fluids 11 (1999) 121–133.
[24] P. Lubin, S. Vincent, S. Abadie, J.P. Caltagirone, Three-dimensional large eddy simulation of air entrainment under plunging breaking waves, Coast. Eng. 53 (2006) 631–655.
[25] A. Iafrati, E.F. Campana, Free surface fluctuations behind microbreakers: space–time behaviour and subsurface flow field, J. Fluid Mech. 529 (2005) 311–347.
[26] A. Iafrati, E.F. Campana, A domain decomposition approach to compute wave breaking, Int. J. Numer. Methods Fluids 41 (2003) 419–445.
[27] J.M. Prusa, P.K. Smolarkiewicz, An all-scale anelastic model for geophysical flows: dynamic grid deformation, J. Comput. Phys. 190 (2003) 601–622.
[28] J. O'Rourke, Computational Geometry in C, Cambridge Univ. Press, 1998, p. 376.
[29] A. Iafrati, A. Di Mascio, E.F. Campana, A level-set technique applied to unsteady free surface flows, Int. J. Numer. Methods Fluids 35 (2001) 281–297.
[30] A. Iafrati, M. Onorato, A. Babanin, Analysis of wave breaking events generated as a result of a modulational instability, in: Proc. 29th ONR Symposium on Naval Hydrodynamics, Gothenburg, Sweden, 26th–31st August 2012.
[31] J.-B. Song, M.L. Banner, On determining the onset and strength of breaking for deep water waves. Part I: Unforced irrotational wave groups, J. Phys. Oceanogr. 32 (2002) 2541–2558.

[32] H.-H. Hwung, W.-S. Chiang, R.-Y. Yang, I.V. Shugan, Threshold model on the evolution of Stokes wave side-band instability, Eur. J. Mech. B, Fluids 30 (2011) 147–155.
[33] M.P. Tulin, Breaking of ocean waves and downshifting, in: J. Grue, J.E. Weber (Eds.), Waves and Nonlinear Processes in Hydrodynamics, Kluwer, 1996, 561 pp.
[34] M.A. Donelan, M.S. Longuet-Higgins, J.S. Turner, Periodicity in whitecaps, Nature 239 (1972) 449–451.
[35] W.K. Melville, F. Veron, C.J. White, The velocity field under breaking waves: coherent structures and turbulence, J. Fluid Mech. 454 (2002) 203–233.
[36] A.D. Drazen, W.K. Melville, Turbulence and mixing in unsteady breaking surface waves turbulence, J. Fluid Mech. 628 (2009) 85–119.
[37] O. Kimmoun, H. Branger, A particle image velocimetry investigation on laboratory surf-zone breaking waves over a sloping beach, J. Fluid Mech. 588 (2007) 353–397.
[38] J. Belden, A.H. Techet, Simultaneous quantitative flow measurement using PIV on both sides of the air–water interface for breaking waves, Exp. Fluids 50 (2011) 149–161.
[39] D. Yang, L. Shen, Simulation of viscous flows with undulatory boundaries: Part II. Coupling with other solvers for two-fluid computations interactions, J. Comput. Phys. 230 (2011) 5510–5531.
[40] N. Reul, N. Branger, J.-P. Giovannangeli, Air flow structure over short-gravity breaking water waves, Bound.-Layer Meteorol. 126 (2002) 477–505.
[41] A.V. Babanin, M.L. Banner, I.R. Young, M.A. Donelan, Wave follower measurements of the wind input spectral function. Part 3. Parameterization of the wind input enhancement due to wave breaking, J. Phys. Oceanogr. 37 (2007) 2764–2775.
[42] A.H. Techet, A.K. McDonald, High speed PIV of breaking waves on both sides of the air–water interface, in: Proc. 6th International Symposium on Particle Image Velocimetry, Pasadena (CA), USA, September 21st–23rd, 2005.
[43] M. Sussman, M.Y. Hussaini, M. Ohta, R. Zhi-Wei, A sharp interface method for incompressible two-phase flows, J. Comput. Phys. 221 (2007) 469–505.